Wideband Low-Profile Dual-Polarized Phased Array with Endfire Radiation Patterns for 5G Mobile Applications

Zhang, Jin; Zhao, Kun; Wang, Lei; Pedersen, Gert Frølund; Zhang, Shuai

Published in:
I E E E Transactions on Vehicular Technology

DOI (link to publication from Publisher):
10.1109/TVT.2021.3095560

Publication date:
2021

Document Version
Accepted author manuscript, peer reviewed version

Wideband Low-Profile Dual-Polarized Phased Array with Endfire Radiation Patterns for 5G Mobile Applications

Jin Zhang, Kun Zhao, Lei Wang, *Member, IEEE*, Gert Frølund Pedersen, *Senior Member, IEEE*, and Shuai Zhang, *Senior Member, IEEE*

***Abstract*—In this paper, an endfire dual-polarized phased array is introduced for 5G mobile applications, which operates from 26 GHz to 30 GHz with low profile of only 1.1 mm ($0.1\lambda_0$ at 26 GHz) and small clearance of 3.5 mm. The array consists of interleaved substrate integrated waveguide (SIW) based vertical-polarized elements and notch type horizontal-polarized elements. The bandwidth of each SIW element is greatly improved by introducing a wide-band impedance transition, which is composed by parallel plate resonators and a metallic via in between. The notch elements have very compact size, which helps to keep the half-wavelength inter-element distance. The array has a planar structure and is easy to fabricate. The measured and simulated results align well with each other.**

***Index Terms*—Dual-polarization, wideband, endfire, 5G, handset antennas.**

I. Introduction

DUAL-POLARIZED arrays are preferred in the cellular communication system for exploring the polarization diversity of propagation channels. There have been many examples of the base station antenna arrays with the dual-polarization feature [1]–[7]. One of the most common methods of exciting dual-polarized radiation is to feed one patch antenna or a pair of identical dipole antennas with orthogonal ports. The dual-polarized radiation can also be realized by exciting orthogonal slots, such as the researches in [8]–[10]. In these works, the dual-polarized antennas usually have the same aperture for both polarization in order to reach a similar performance.

For the 5th generation (5G) cellular system, particularly in the millimeter-wave (mm-wave) spectrum, the dual-polarized array is involved not only in the base stations, but also in the mobile devices. The antenna design for the mobile devices suffers different challenges compared to the base station (BS) antennas. For example, mobile device antennas have to face a stricter size limitation and a more complicated electromagnetic environment, while they are still required to cover a large bandwidth and spatial coverage simultaneously. Moreover, mm-wave handset arrays with endfire radiation patterns are highly preferred in practical applications due to their large spatial coverage [11]. Endfire arrays with low profile structure for 5G mm-wave handset applications are proposed in [12]–[14] with horizontal polarization. However, it is very challenging to design the endfire dual-polarized arrays for mobile terminals, mainly due to the difficulty of obtaining a sufficient bandwidth with a thin planar structure for the vertical polarization. Furthermore, the concept of clearance is defined for measuring the total footprint of the antenna structure on the ground plane [15]. The antennas with smaller clearance are easier to be integrated inside the mobile phone.

Examples of dual-polarized arrays with endfire radiation patterns can be found in [16]–[22]. The planar dual-polarized antenna design with a low profile, such as in [16], has a relatively narrow bandwidth, while the wideband designs, e.g., in [17], [18], have a relatively high profile. In addition, [17] requires a 180^o hybrid for the differential feeding and [18], [19] have a large inter-element distance. In [21], [22], the dual-polarized arrays are implemented on the metal bezel of the mobile phone, which require a metal reflector behind for the endfire radiation. In order to optimize the space utilization, some researches have combined two different types of antennas for the two polarization. In [20], the horizontal polarization (H-pol) is realized by dipole antennas and the vertical polarization (V-pol) is achieved by monopole antennas, which reduces the required height for V-pol but it still has a large clearance.

Endfire H-plane antennas based on SIW are good candidates for V-pol radiation due to the advantage of the planar structure and the compatibility with printed circuit boards (PCBs). Many methods are presented in order to improve the impedance matching and bandwidth, such as loading with dielectric lens [23]–[27], extending the metal with a tapered edge [23], introducing a ridge inside the SIW [28], and loading of transition plates [25], [29], [30] or metamaterial [31]. Among these methods, the loading of transition plates are applied in many SIW antenna designs due to the compact size and easily combining with the other technologies [32]–[34].

However, many of those designs are not suitable for the array applications in a mobile phone environment. Most of the H-plane horn antennas require a large element separation

This work was supported by the AAU Young Talent Program and in part by the Innovations Fonden Project of RANGE (Corresponding author: Shuai Zhang).

J. Zhang, S. Zhang (e-mail: sz@es.aau.dk), K. Zhao, and G. F. Pedersen are with the Antennas, Propagation and Millimeter-wave Systems, Department of Electronic Systems, Aalborg University, 9220 Aalborg Ø, Denmark.

K. Zhao is also with Sony Research Center, Lund, Sweden.

L. Wang is with the School of Engineering and Physical Sciences, Institute of Sensors, Signals and Systems, Heriot-Watt University, EH14 4AS, United Kingdom (e-mail: Lei.Wang@hw.ac.uk).

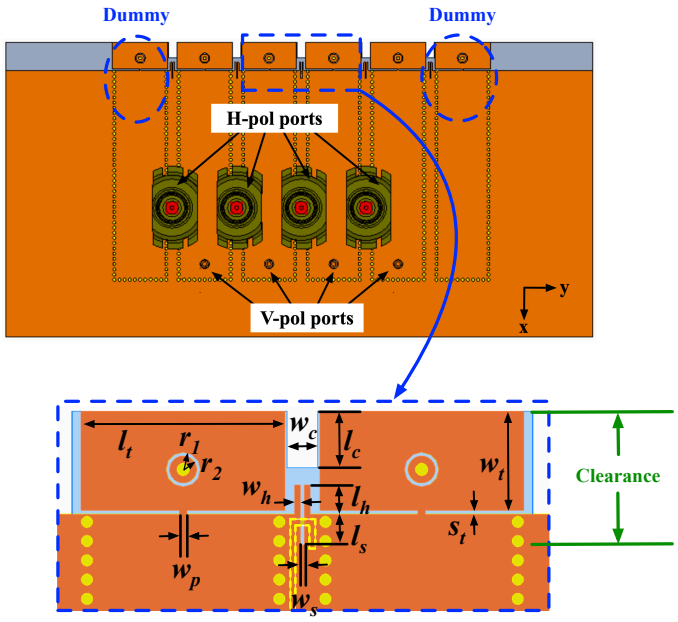

(a)

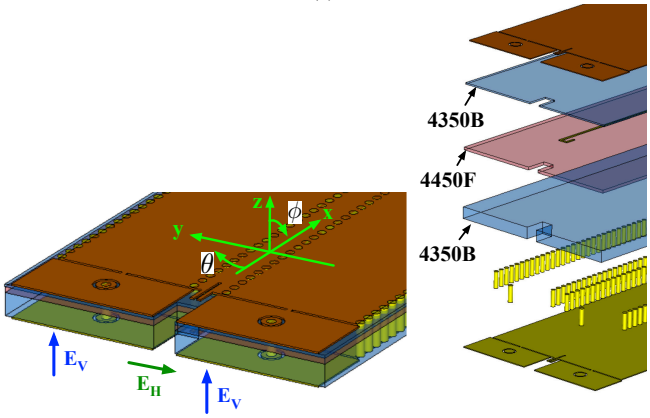

(b) (c)

Fig. 1: Array configuration. (a) Array configuration and dimensions. (b) Perspective view of array elements. (c) Explored view of layers. (l_t = 5.3 mm, w_t = 2.57 mm, l_c = 1.47 mm, w_c = 0.8 mm, s_t = 0.1 mm, w_h = 0.15 mm, l_h = 0.75 mm, l_s = 0.8 mm, w_s = 0.1 mm, w_p = 0.1 mm, r_1 = 0.5 mm, r_2 = 0.4 mm.)

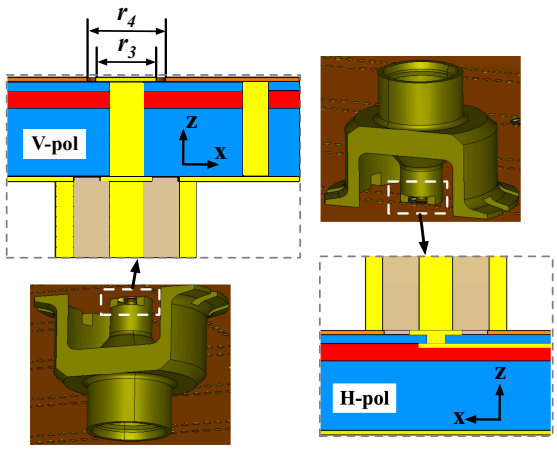

Fig. 2: Feeding ports of V-pol and H-pol array elements. (r_3 = 0.35 mm, r_4 = 0.45 mm.)

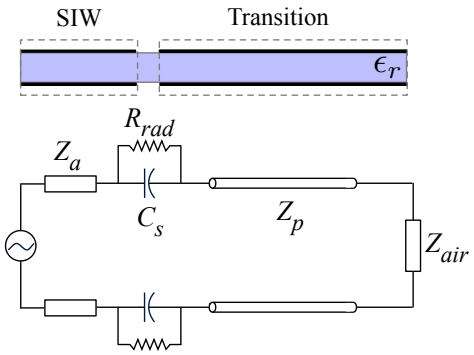

(a)

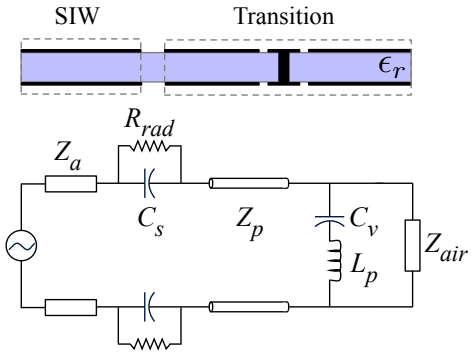

(b)

Fig. 3: TL models. (a) Conventional transition plate (Model-A). (b) Propoesed transition plate with metallic via (Model-B).

due to the wide opening [35], and the loading of dielectric lens or transition plates demands a large clearance. In [36], the transition plates of the endfire SIW antennas are modified to generate the H-pol radiation, which is suitable for the array applications and has a small clearance, but the narrow bandwidth of the V-pol has limited its potential for 5G wideband applications.

Therefore, it is necessary and challenging to find a solution, which can improve the bandwidth of endfire V-pol radiation while still maintaining a low profile, small clearance, and array inter-element distance. In this paper, we propose a dual-polarized endfire phased array for 5G mobile applications, which combines the SIW antennas and the notch antennas. The major novelties of this work are two fold. Firstly, a novel wideband transition structure for SIW antenna over a thin substrate is introduced to broaden the bandwidth of V-pol antennas. The wideband transition is composed by a pair of parallel plate resonators with a metal via in-between, which provides a dual-resonant matching through a simple and compact structures without further increasing the antenna clearance. Secondly, the miniaturized notch antennas are integrated between the SIW elements for H-pol radiation. Such a configuration represents a novel way to integrate dual-polarized antenna array, which minimizes the clearance and the array inter-element distance. In this way, the V-pol and H-pol reach the same operating band from 26 GHz to 30 GHz. The clearance is 3.5 mm and

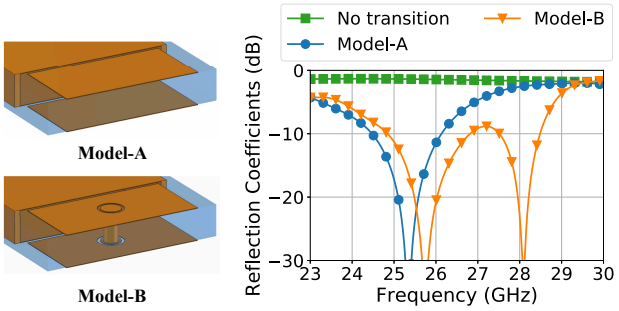

Fig. 4: Reflection coefficients of the SIW antenna with conventional transition plate (Model-A) and with proposed transition plate (Model-B).

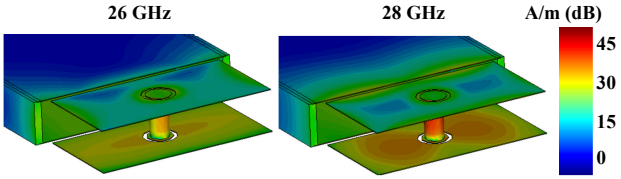

Fig. 5: Average surface current distribution of Model-B.

the profile (or the substrate thickness) is only 1.1 mm, which is compatible with the modern mobile phone environment.

The paper is organized as follows: Section II introduces the configuration of the proposed dual-polarized array; Section III explains the design and the operating principle of the wideband low-profile V-pol antenna; Section IV presents the integration of the H-pol antennas into the V-pol array; Section V demonstrates the performances of the dual-polarized array; Section VI shows the measurement results and discussions; and the conclusions are drawn in Section VII.

II. Dual-Polarized Array Structure

Fig. 1(a) shows the configuration and dimensions of the proposed array, which includes four V-pol elements, four H-pol elements, and three dummy elements. The array elements of V-pol and H-pol are placed interleaved. The V-pol elements are realized by wideband low-profile SIW antennas and the H-pol elements are miniaturized notch antennas. The operating principle of the V-pol and H-pol antenna will be explained in section III and IV, respectively.

Fig. 1(b) shows the perspective view of the array elements. The array is constructed by a two-layer stacked substrate of Rogers 4350B with a thickness of 0.8 mm and 0.1 mm, respectively. The dielectric constant is 3.66 and the tanδ is 0.0037. The two layers are attached by a 0.2 mm thick prepreg of Rogers 4450F, which has a dielectric constant of 3.7 and tanδ of 0.004. The width of the SIW is 5 mm and the inter-element distance is 6.2 mm.

The elements are fed with coaxial type MMPX connectors on the two sides of the PCB. The transitions from the connectors to the stripline and the SIW are shown in Fig. 2. For the V-pol elements, the SIW is excited by a probe transition through the connector. For the H-pol elements, the inner conductor of the connector is directly connected to the stripline through a via.

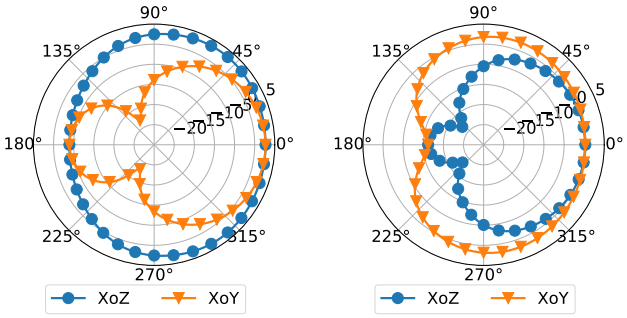

Fig. 6: Radiation pattern of V-pol at (a) 26 GHz. (b) 28 GHz.

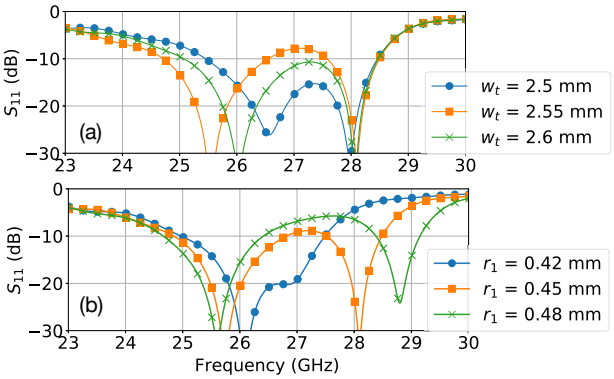

Fig. 7: Reflection coefficients of Model-B with different (a) w_t and (b) r_1.

III. Wideband Low-Profile SIW Antenna Design

A. Working Princeple

The transition plates located at the antenna-air interface of the SIW antenna are proposed in [37] for smoothing the impedance difference between the SIW and the air. The transmission line (TL) model of such a transition structure (Model-A) is shown in Fig. 3(a). The transition part can be seen as a quarter wavelength resonator, which is constructed by a open-ended parallel plate waveguide with characteristic impedance of Z_p. The Z_a and Z_{air} are the equivalent impedance of the SIW and the air, respectively. The C_s and R_{rad} are the coupling capacitance and the radiation resistance of the slot between the SIW and the transition plates. Therefore, the antenna with one pair of transition plates can achieve one resonant frequency. Concatenating multiple pairs of transition plates can increase the bandwidth by enabling more resonant frequencies. However, such a method comes with a cost of increasing the antenna clearance, which may not be feasible for mobile applications.

Therefore, we propose an improved impedance matching method with the transition plates (Model-B). The equivalent circuit is shown in Fig. 3(b). A metallic via is added in order to introduce an inductance L_p between the two transition plates. In addition, a loop slot is etched on each transition plate surrounding this via, which forms a coupling capacitance C_v. As a result, the inductance L_p and the capacitance C_v generates one more resonance that only depends on the dimensions of the via and the slot. Compared to Model-A, Model-B is

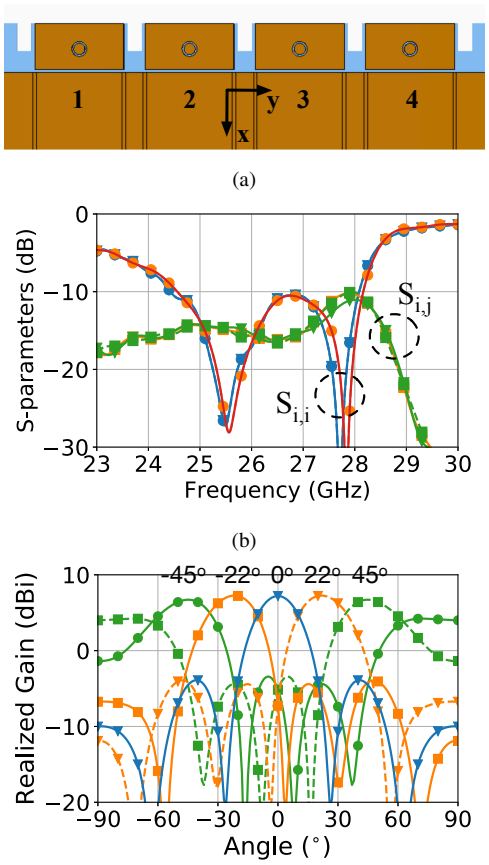

Fig. 8: 1×4 array with the proposed of V-pol antenna elements. (a) Configuration of the 1×4 V-pol array. (b) S-parameters (i = 1, 2, 3, 4, and j = 2, 3, 4). (c) Scanning patterns at 27 GHz.

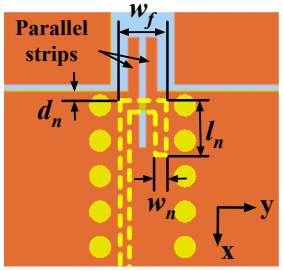

Fig. 9: Feeding structure of the notch antenna. (w_f = 0.7 mm, d_n = 0.1 mm, l_n = 0.78 mm, w_n = 0.15 mm.)

capable of achieving a wider bandwidth by merging these two resonances: one from the transition plates and the other one from the metallic via.

The reflection coefficients of Model-A and Model-B are shown in Fig. 4. Both models are simulated as a single antenna in the free space with open boundary. The result of the model without transition plate is also shown for comparison. Model-A and Model-B have a common resonance between 25 GHz and 26 GHz, which comes from the effect of the transition plates. Model-B has one more resonance at 28 GHz, which corresponds to the effect of the metallic via. Compared with Model-A, Model-B has reached a much wider bandwidth,

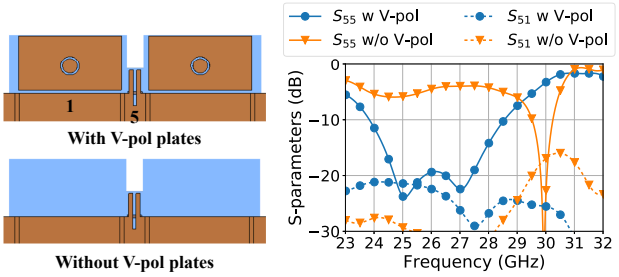

Fig. 10: S-parameters of H-pol antenna with and without V-pol transition plates.

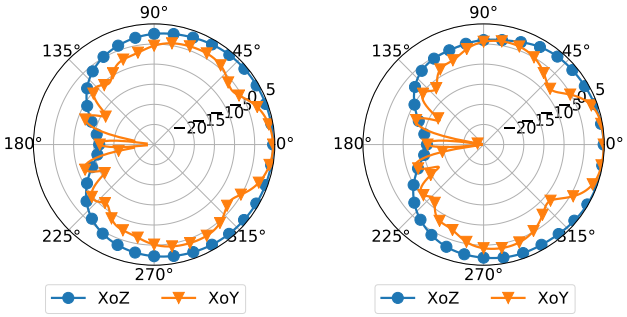

Fig. 11: Radiation pattern of H-pol at (a) 26 GHz. (b) 28 GHz.

while the profile and the size of the transition plates are the same.

Fig. 5 shows the average surface current distribution of Model-B. At 26 GHz, the current distributes more evenly on the transition plates and not significantly on the via, while it is much stronger on the via at 28 GHz. Fig. 6 shows the radiation patterns at 26 GHz and 28 GHz. Both frequencies have endfire radiation patterns with broad beamwidth. The cross-polarization is very low. The realized gain is 3.5 dBi at 26 GHz and 2 dBi at 28 GHz.

B. Parametric Study

In Model-B, the two resonant frequencies can be tuned separately. As shown in Fig. 7(a), the lower resonance can be controlled by the length of the transition plate w_t without significantly changing the higher resonance. In Fig. 7(b), the higher resonance can be easily controlled by the coupling capacitance C_v, which corresponds to the slot width $r_1 - r_2$. When r_2 is fixed, the frequency of the higher resonance becomes lower as r_1 becoming smaller. Meanwhile, the tuning of r_1 has a minor influence on the lower resonance as well because the loop slot impacts the equivalent impedance of the transition plates. The bandwidth of the V-pol antenna becomes wider when the two resonances are more separated, while the reflection between the two resonances increases.

C. V-pol Array Performance

Fig. 8(a) shows a 1×4 array with the proposed V-pol antenna as the array element. The inter-element distance is 6.2 mm. The reflection coefficients and the mutual coupling

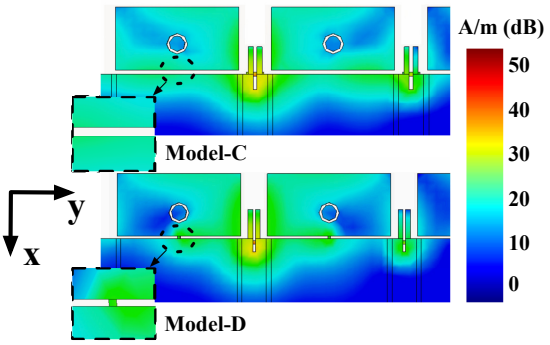

(a)

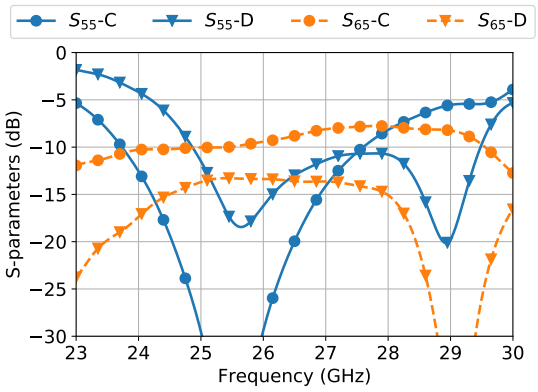

(b)

Fig. 12: Surface current and S-parameters of H-pol with or without the decoupling strip. (a) Average surface current distribution at 25.5 GHz. (b) S-parameters.

between the adjacent elements are shown in Fig. 8(b). The coupling will reduce after adding the H-pol elements. The scanning pattern in the XoY plane at 27 GHz are shown in Fig. 8(c). The scanning angle is from -45^o to 45^o and the gain ranges from 6.7 dBi to 7.3 dBi. The active reflection coefficients (ARC) of each element is below -9.3 dB at array scan angle of 45^o. The scanning patterns are similar over the operating band.

IV. H-POL ANTENNA INTEGRATION

A. Integration and operating principle of H-pol antenna element

The V-pol array in the previous section can already achieve a decent performance with a compact dimension. However, in order to realize the dual-polarized operation, an endfire H-pol array shall be integrated as well. In order to minimize the total footprint of the dual-polarized antenna, an H-pol array is preferred with compact size and easy integration between the V-pol antennas.

Notch antennas provide endfire radiation and have the advantage in terms of integration. In our design, the notch antenna, as shown in Fig. 1(b), is integrated between the SIW elements in order to provide H-pol radiation. It is fed by an open ended stripline, as shown in Fig. 9.

The transition plates of the SIW antennas can be seen as parasitic loadings to the notch antenna, which helps the notch

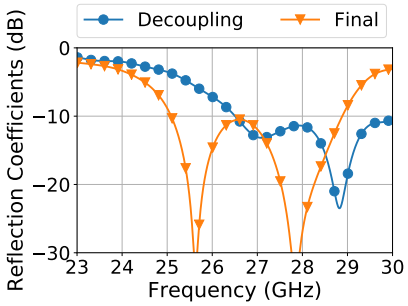

(a)

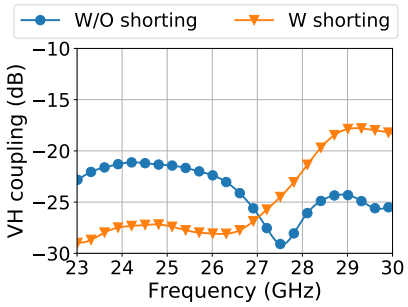

(b)

Fig. 13: Impact on the V-pol antenna. (a) Reflection coefficients of V-pol with and without the shorting point. (b) Mutual coupling between V-pol and H-pol with the shorting point.

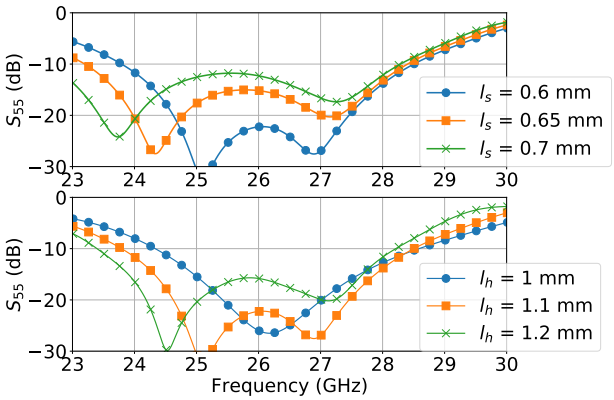

Fig. 14: Reflection coefficients of Model-D with different l_s and l_h.

antenna to gain a good impedance matching and broaden the bandwidth. Fig. 10 shows the comparison of the notch antenna performance with and without the SIW transition plates. Port 1 and Port 5 are the adjacent V-pol and H-pol ports, respectively. When the notch antenna operates without the transition plates, it has a very narrow matching band at 30 GHz. When the transition plates are loaded, the impedance matching from 24 GHz to 28.5 GHz is significantly improved. The mutual coupling between the V-pol and H-pol ports is lower than -20 dB after loading the transition plates. The radiation patterns of the proposed H-pol antenna at 26 GHz and 28 GHz are shown in Fig. 11. The realized gain is 4.6 dBi and 4.9 dBi, respectively. The cross-polarization is below -15 dB.

B. Mutual Coupling Reduction of H-pol Antennas and Impact on V-pol Antennas

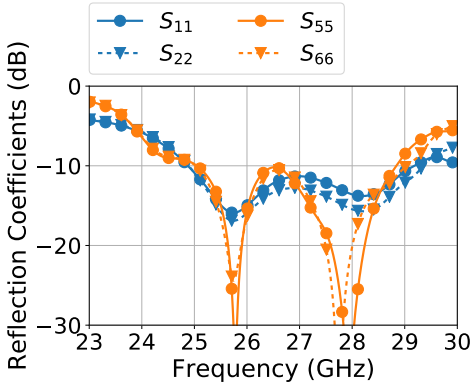

(a)

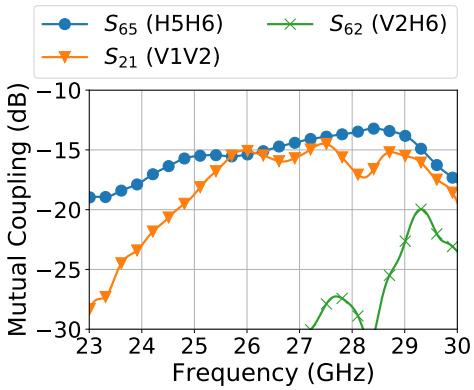

(b)

Fig. 15: S-parameters of the array elements V1, V2, H5, and H6. (a) Reflection coefficients. (b) Mutual coupling.

In order to reduce the mutual coupling between the H-pol elements, the middle of the SIW transition plate is shorted to the ground plane. Fig. 12 shows the average surface current distribution at 25.5 GHz and the S-parameters of the two cases without the shorting (Model-C) and with the shorting (Model-D). To be noted, some structure parameters in Model-D are slightly optimized in order to reach a good impedance matching of H-pol. As to be seen, the surface current in Model-C spreads widely along y-axis direction, while it is much constrained between the two shorting points in Model-D. As a result, the coupling between the two adjacent H-pol ports is decreased by 3 to 4 dB.

However, integration of the H-pol antennas, has a non-negligible impact on the impedance matching of V-pol antennas. It becomes particularly critical when the V-pol transition plates need to be shorted in order to reduce the mutual coupling of H-pol. It can be observed in Fig. 13(a), where the "Decoupling" shows the impedance matching after the SIW transition plate is shorted to the ground plane. In this case, the V-pol impedance matching is strongly influenced. Therefore, the structure parameters of the V-pol antenna have to be optimized in order to compensate for the impact. The "Final" shows the reflection coefficients of the V-pol antenna after optimizing, where a good impedance matching is reached. The structure parameters of "Final" are obtained according to those listed in Fig. 1. At the same time, the slightly tuning of the V-pol antenna structure parameters has no significant influence on the H-pol antenna.

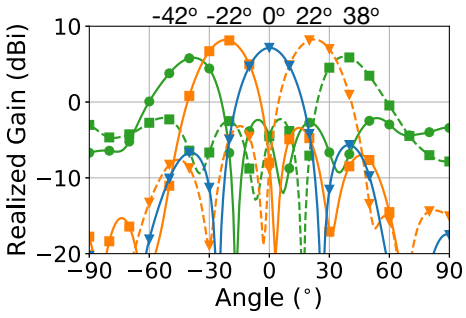

(a)

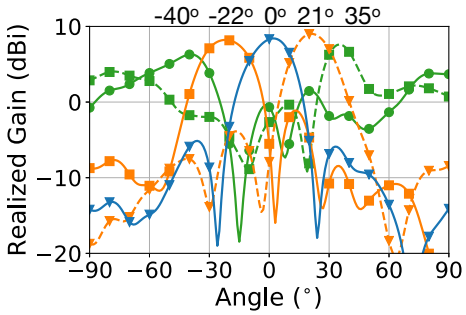

(b)

Fig. 16: Simulated beam scanning pattern in xoy plane at 27 GHz. (a) V-pol. (b) H-pol.

Introducing of the shorting point has little impact on the V-pol and H-pol coupling. Fig. 13(b) shows the mutual coupling of the adjacent V-pol and H-pol ports with and without the shorting point. In both cases, the impedance matching of the V-pol and H-pol antennas are good. Based on this, the coupling is below -17 dB over the whole operating band.

C. Parametric Study

The resonant frequencies of the notch antenna can be tuned by the slot length (l_s) and the strip length (l_h). As shown in Fig. 14, the frequency of the lower resonance moves higher when l_s becomes shorter. As shown in Fig. 14(b), the two resonances moves closer when l_h becomes shorter. The bandwidth becomes larger when the frequencies of the two resonances are more separated.

V. Dual-Polarized Array Performances

A. Impedance Bandwidth

The operation mechanism of each polarized antenna element and the design flow of the dual polarized array have been explained in previous sections. Here, the performance of the final design of the dual-polarized array are given. Fig. 15 shows the reflection coefficients of the elements V1, V2, and H5, H6 (see Fig. 1), and the mutual coupling between the adjacent elements V1 and V2, H5 and H6, V2 and H6. The

array elements have similar performance and the operating band of both V-pol and H-pol covers from 25 GHz to 29 GHz. The mutual coupling between the adjacent ports of the same polarization is below -13 dB and of the different polarization is below -20 dB over the operating band.

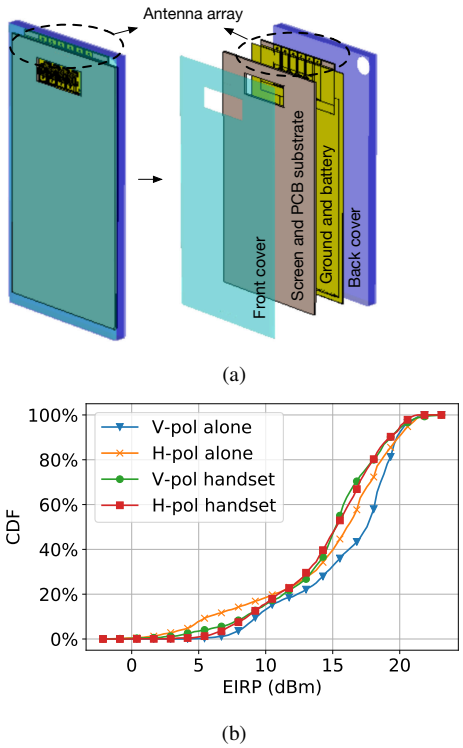

Fig. 17: Spherical coverage of the proposed array alone and inside a handset device model. (a) Simulation model of the proposed antenna array in the handset model. (b) Spherical coverage of V-pol and H-pol at 27 GHz (The accepted power at each polarized array is set to be 13 dBm.

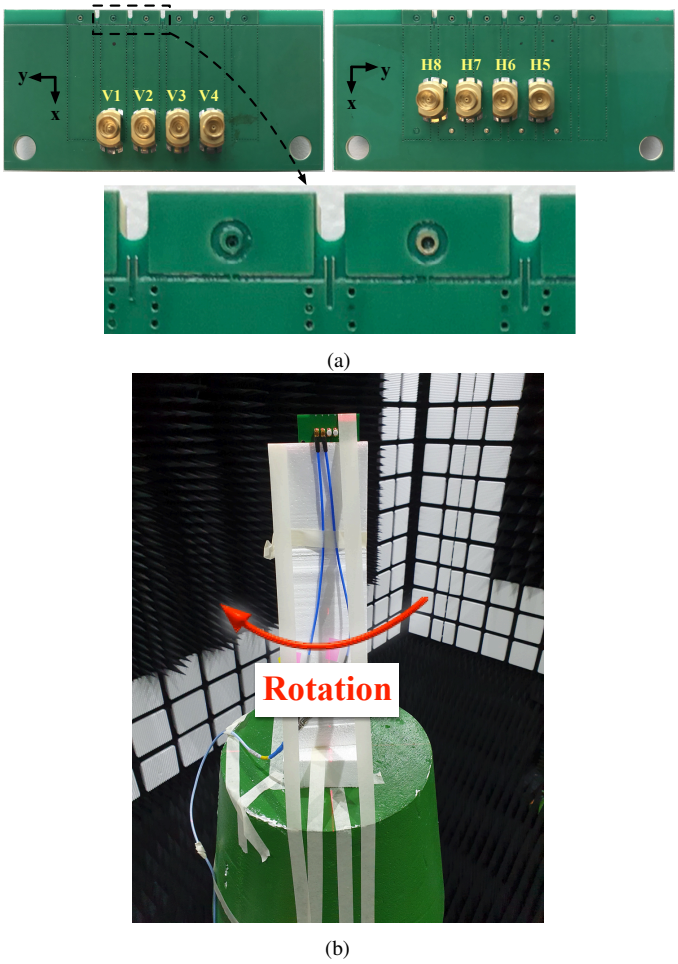

Fig. 18: Photograph of the fabricated antenna and the measurement setup. (a) Fabricated antenna configuration. (b) Measurement setup.

B. Beam scanning angle, total efficiency, and spherical coverage

Fig. 16 shows the beam scanning patterns in the XoY plane at 27 GHz. The scanning angle of V-pol is from -42^o to 38^o and the realized gain ranges from 6 dBi to 8.2 dBi. The scanning angle of H-pol is from -40^o to 35^o and the realized gain ranges from 6.3 dBi to 9 dBi. The total efficiency of each array element ranges from -1 dB to -2 dB.

As we mentioned previously, the spherical coverage is a critical performance for the mm-wave mobile devices. Therefore, the spherical coverage of the proposed array has also been presented here. The array is simulated alone and inside a mobile device model, respectively, as shown in Fig.17(a). The handset model consists of a front cover ($\epsilon_r = 6.84$, $tan\delta = 0.0297$), a simplified model for screen and phone PCB substrate ($\epsilon_r = 4.82$, $tan\delta = 0.0054$), a ground plane and battery (both modeled as copper), and a back cover ($\epsilon_r = 3$). The uplink spherical coverage is measured by the Cumulative Distribution Function (CDF) of the Equivalent Isotropically Radiated Power (EIRP), according to the 3GPP specification [38]. For obtaining the spherical coverage of the proposed array, five beams of each case are adopted. The accepted power of each polarized array is set to be 13 dBm. The EIRP is proportional to the antenna realized gain obtained from our simulations. The spherical coverage of the proposed array at 27 GHz is shown in Fig. 17(b). When the array operates alone, the coverage of the V-pol is slightly larger than that of the H-pol. In the handset device, the coverage of the two poalrization becomes similar. Even though, the array coverage in the handset device slightly decreases at high EIRP, both cases and polarization have met the requirements of the handheld mobile devices for operating band n257 and n258 of minimum peak EIRP of 22.4 dBm at CDF of 100% and 11.5 dBm at CDF of 50% with the assumed accepted power, according to the 3GPP specification [38].

VI. Measurements and Discussions

The photograph of the fabricated array model is shown in Fig. 18(a). Fig. 18(b) shows the radiation pattern measurement setup in the anechoic chamber. The antenna is mounted on a platform, which rotates along the ϕ-axis. The measuring probe moves along θ-axis from 0^o to 155^o.

Fig. 19 shows the simulated and measured reflection coefficients of the V-pol elements V3, V4, and the H-pol elements

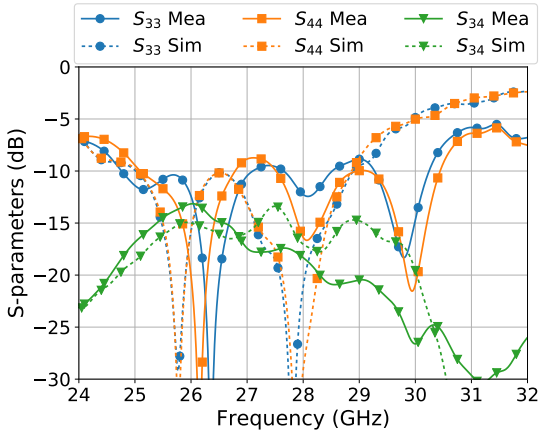

(a)

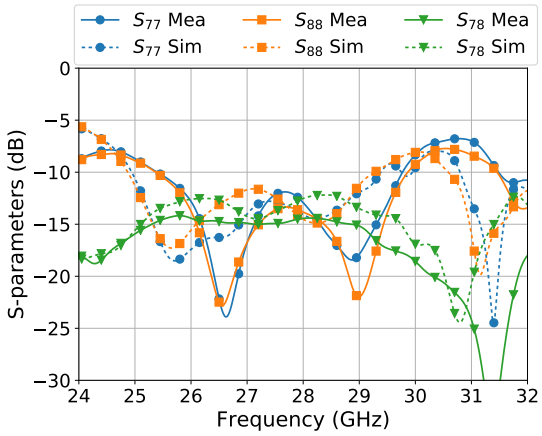

(b)

Fig. 19: Measured and simulated S-parameters of the array elements V3, V4, H7, and H8. (a) V-pol (Port 3 and Port 4). (b) H-pol (Port 7 and Port 8).

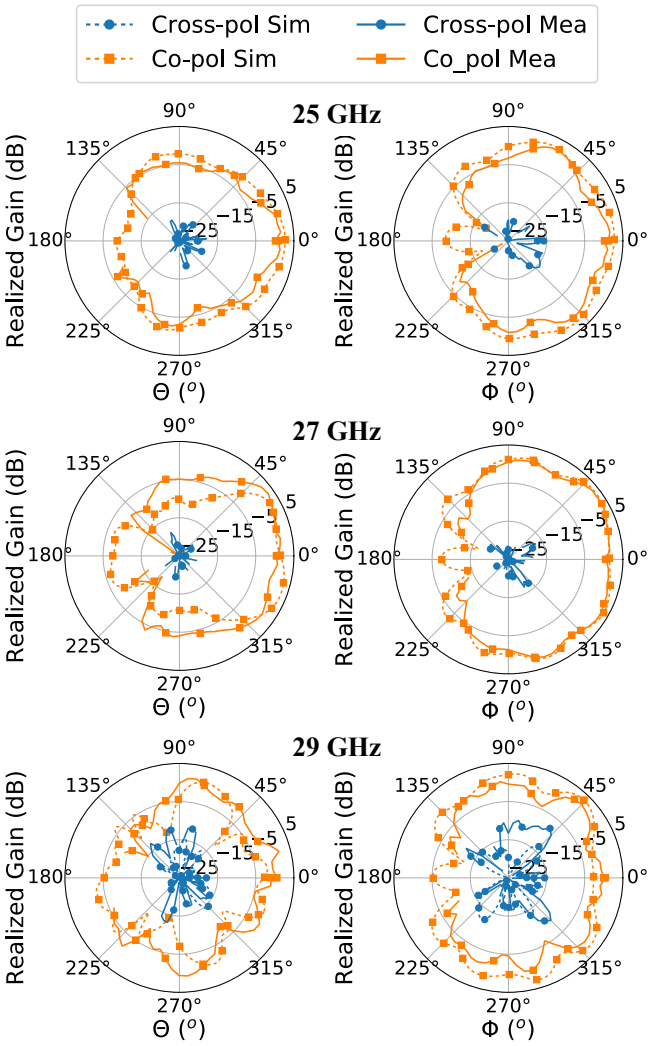

Fig. 20: Simulated and measured radiation patterns of V3 at 25 GHz, 27 GHz and 29 GHz.

H7, H8, and the mutual coupling between the V-pol element V3 and V4, and the H-pol elements H7 and H8. The ports V1, V2, H5, and H6 are left open during the measurement. However, the isolation between antenna ports is high enough to avoid obvious influence on the results of the measuring ports. The operating band is slightly higher in the measurement compared to the simulations due to the fabrication errors, but both polarization still cover from 25 GHz to 29 GHz. The mutual coupling between the elements of the same polarization is lower than -13 dB in both simulations and measurements.

The radiation patterns are measured on both Φ and Θ planes (Fig. 1(a)). Fig. 20 and Fig. 21 demonstrate the simulated and measured radiation patterns from 25 GHz to 29 GHz of the V-pol and the H-pol elments (V3 and H7), respectively. The measured radiation patterns are similar to the simulated results. The simulated realized gain of the V-pol ranges from 2.16 dBi to 3.74 dBi and of the H-pol ranges from 3.7 dBi to 5 dBi. The measured realized gain of the co-polarization of the V-pol elements ranges from 1.85 dBi to 2.48 dBi and of the H-pol elements ranges from 3.51 dBi to 5.9 dBi. The cross-polarization increases as the frequency increasing due to the effect of the surface current.

Table I shows the comparison of the proposed antenna array and the other dual-polarized endfire antennas with planar structure based on the measured results. The proposed array has achieved the smallest thickness of only $0.1\lambda_0$, but the bandwidth is much larger than [16] and [36]. Compared to the wideband designs in [17], [18], [20], [35], the proposed design provides the smallest element separation, which guarantees to a larger scanning angle. Besides, the proposed array has a relatively small clearance and a low cross-polarization level. To be noticed, the clearance of the proposed array is slightly larger than that in [36], but it is determined by the H-pol antennas. The clearance of the V-pol antennas is identical as [36]. Also compared with [36], the proposed array has slightly lower element gain. It is due to the broader beam, which, in fact, gives a better coverage.

VII. Conclusion

This paper proposes a wideband endfire dual-polarized antenna array for 5G mobile applications. The array operates from 26 GHz to 30 GHz for both polarization. A novel

TABLE I
COMPARISON WITH OTHER DUAL-POLARIZED ENDFIRE MM-WAVE ANTENNAS WITH PLANAR STRUCTURE.

Ref No.	Pol.	Ele. Num.	BW	Ele. Gain	Cross-pol.	Scanning range	W × C × T (λ_0)
[16]	LP/LP	1	8.6%	$4-5$ dBi	-15 dB	Not array	$0.74 \times 0.28 \times 0.18$
[17]	LP/LP	1	22%	$5-6$ dBi	-12 dB	Not array	$0.58 \times 0.41 \times 0.36$
[20]	LP/LP	1×4	25%	6.5 dBi	-17 dB	Not given	$0.86 \times 1.54 \times 0.23$
[18]	LP/LP	1×8	21%	$6-7$ dBi	-30 dB	-25^o to 25^o	$0.77 \times 0.53 \times 0.47$
[35]	LP/LP	1×4	18.5%	$3-4$ dBi	-10 dB	-34^o to 33^o	$1 \times 0.16 \times 0.19$
[36]	LP/LP	1×4	7%	5 dBi	-10 dB	-42^o to 33^o	$0.51 \times 0.28 \times 0.1$
This work	LP/LP	1×4	14.8%	$2-5$ dBi	-15 dB	-40^o to 35^o	$0.57 \times 0.32 \times 0.1$

*BW: relatively bandwidth ($(f_H - f_L)/f_0$). W × C × T: Width × Clearance × Thickness.

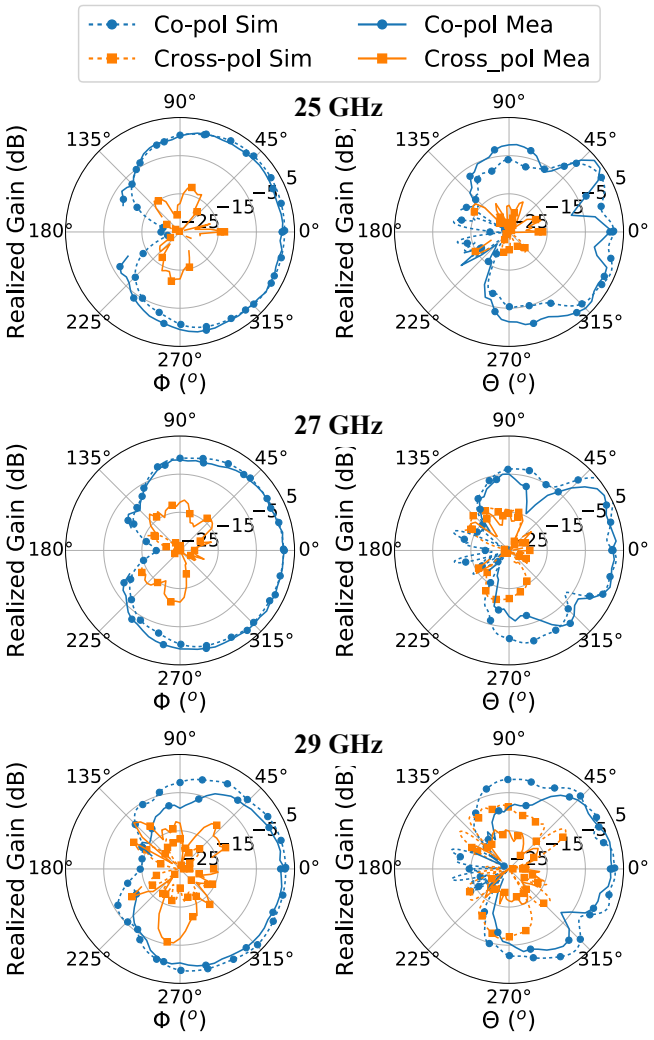

Fig. 21: Simulated and measured radiation patterns of H7 at 25 GHz, 27 GHz and 29 GHz.

wideband transition is introduced for the SIW antenna, which has immensely broadened the bandwidth of the V-pol elements without increasing the thickness. The notch-type H-pol elements are miniaturized and integrated between the V-pol elements. The proposed array has a planar structure, which has a very low profile of 1.1 mm and a small clearance of 3.5 mm. It is compatible with the thin PCB in the 5G mobile phones. The measurement results match well with the simulations.

REFERENCES

[1] Y. Cui, L. Wu, and R. Li, "Bandwidth enhancement of a broadband dual-polarized antenna for 2G/3G/4G and IMT base stations," *IEEE Trans. Antennas Propag.*, vol. 66, no. 12, pp. 7368–7373, Aug. 2018.

[2] S. Zhang, X. Chen, and G. F. Pedersen, "Mutual coupling suppression with decoupling ground for massive mimo antenna arrays," *IEEE Transactions on Vehicular Technology*, vol. 68, no. 8, pp. 7273–7282, Jun. 2019.

[3] C. Ding, H. Sun, R. W. Ziolkowski, and Y. Jay Guo, "A dual layered loop array antenna for base stations with enhanced cross-polarization discrimination," *IEEE Trans. Antennas Propag.*, vol. 66, no. 12, pp. 6975–6985, Sep. 2018.

[4] Z. Tang, J. Liu, Y. Cai, J. Wang, and Y. Yin, "A wideband differentially fed dual-polarized stacked patch antenna with tuned slot excitations," *IEEE Trans. Antennas Propag.*, vol. 66, no. 4, pp. 2055–2060, Feb. 2018.

[5] C. F. Ding, X. Y. Zhang, Y. Zhang, Y. M. Pan, and Q. Xue, "Compact broadband dual-polarized filtering dipole antenna with high selectivity for base-station applications," *IEEE Trans. Antennas Propag.*, vol. 66, no. 11, pp. 5747–5756, Aug. 2018.

[6] L. Y. Nie, X. Q. Lin, Y. J. Chen, J. Zhang, B. Wang, Z. Q. Yang, and Y. Fan, "A low-profile coplanar dual-polarized and dual-band base station antenna array," *IEEE Trans. Antennas Propag.*, vol. 66, no. 12, pp. 6921–6929, Sep. 2018.

[7] T. P. Wong and K. M. Luk, "A wide bandwidth and wide beamwidth cdma/gsm base station antenna array with low backlobe radiation," *IEEE Transactions on Vehicular Technology*, vol. 54, no. 3, pp. 903–909, May 2005.

[8] X. Qin and Y. Li, "Compact dual-polarized cross-slot antenna with colocated feeding," *IEEE Trans. Antennas Propag.*, vol. 67, no. 11, pp. 7139–7143, Aug. 2019.

[9] G. Srivastava and A. Mohan, "A differential dual-polarized SIW cavity-backed slot antenna," *IEEE Trans. Antennas Propag.*, vol. 67, no. 5, pp. 3450–3454, Feb. 2019.

[10] M. Li, R. Wang, J. M. Yasir, and L. Jiang, "A miniaturized dual-band dual-polarized band-notched slot antenna array with high isolation for base station applications," *IEEE Trans. Antennas Propag.*, vol. 68, no. 2, pp. 795–804, Sep. 2020.

[11] K. Zhao, S. Zhang, Z. Ho, O. Zander, T. Bolin, Z. Ying, and G. F. Pedersen, "Spherical coverage characterization of 5G millimeter wave user equipment with 3GPP specifications," *IEEE Access*, vol. 7, pp. 4442–4452, Dec. 2019.

[12] M. M. Samadi Taheri, A. Abdipour, S. Zhang, and G. F. Pedersen, "Integrated millimeter-wave wideband end-fire 5g beam steerable array and low-frequency 4g lte antenna in mobile terminals," *IEEE Transactions on Vehicular Technology*, vol. 68, no. 4, pp. 4042–4046, Feb. 2019.

[13] H. Ozpinar, S. Aksimsek, and N. T. Tokan, "A novel compact, broadband, high gain millimeter-wave antenna for 5g beam steering applications," *IEEE Transactions on Vehicular Technology*, vol. 69, no. 3, pp. 2389–2397, Jan. 2020.

[14] R. Rodriguez-Cano, K. Zhao, S. Zhang, and G. F. Pedersen, "Handset frame blockage reduction of 5g mm-wave phased arrays using hard surface inspired structure," *IEEE Transactions on Vehicular Technology*, vol. 69, no. 8, pp. 8132–8139, May 2020.

[15] J. Zhang, S. Zhang, Z. Ying, A. S. Morris, and G. F. Pedersen, "Radiation-pattern reconfigurable phased array with pin diodes controlled for 5g mobile terminals," *IEEE Transactions on Microwave Theory and Techniques*, vol. 68, no. 3, pp. 1103–1117, Dec. 2019.

[16] M. Esquius-Morote, M. Mattes, and J. R. Mosig, "Orthomode transducer and dual-polarized horn antenna in substrate integrated technology," *IEEE Trans. Antennas Propag.*, vol. 62, no. 10, pp. 4935–4944, Oct. 2014.

[17] A. Li and K. Luk, "Millimeter-wave dual linearly polarized endfire antenna fed by 180^o hybrid coupler," *IEEE Antennas Wirel. Propag. Lett.*, vol. 18, no. 7, pp. 1390–1394, Jul. 2019.

[18] A. Li, K. Luk, and Y. Li, "A dual linearly polarized end-fire antenna array for the 5G applications," *IEEE Access*, vol. 6, pp. 78 276–78 285, Dec. 2018.

[19] A. Li and K. Luk, "Single-layer wideband end-fire dual-polarized antenna array for device-to-device communication in 5g wireless systems," *IEEE Transactions on Vehicular Technology*, vol. 69, no. 5, pp. 5142–5150, Mar. 2020.

[20] Y. Hsu, T. Huang, H. Lin, and Y. Lin, "Dual-polarized quasi Yagi–Uda antennas with endfire radiation for millimeter-wave MIMO terminals," *IEEE Trans. Antennas Propag.*, vol. 65, no. 12, pp. 6282–6289, Jul. 2017.

[21] R. M. Moreno, J. Ala-Laurinaho, A. Khripkov, J. Ilvonen, and V. Viikari, "Dual-polarized mm-wave end-fire antenna for mobile devices," *IEEE Trans. Antennas Propag.*, pp. 1–1, Apr. 2020.

[22] R. M. Moreno, J. Kurvinen, J. Ala-Laurinaho, A. Khripkov, J. Ilvonen, J. van Wonterghem, and V. Viikari, "Dual-polarized mm-wave end-fire chain-slot antenna for mobile devices," *IEEE Transactions on Antennas and Propagation*, pp. 1–1, Jun. 2020.

[23] Y. Zhao, Z. Shen, and W. Wu, "Wideband and low-profile H-plane ridged SIW horn antenna mounted on a large conducting plane," *IEEE Trans. Antennas Propag.*, vol. 62, no. 11, pp. 5895–5900, Sep. 2014.

[24] N. Ghassemi and K. Wu, "Planar high-gain dielectric-loaded antipodal linearly tapered slot antenna for E- and W-band gigabyte point-to-point wireless services," *IEEE Trans. Antennas Propag.*, vol. 61, no. 4, pp. 1747–1755, Jan. 2013.

[25] W. B. Park, J. M. Lee, S. Lee, Y. M. Park, and K. C. Hwang, "A 18–40 GHz substrate integrated waveguide H-plane horn antenna," *IEEE Trans. Antennas Propag.*, vol. 66, no. 11, pp. 6322–6327, Aug. 2018.

[26] Y. Cai, Z. Qian, Y. Zhang, and W. Cao, "A compact wideband SIW-fed dielectric antenna with end-fire radiation pattern," *IEEE Trans. Antennas Propag.*, vol. 64, no. 4, pp. 1502–1507, Jan. 2016.

[27] Y. Cai, Z. Qian, W. Cao, Y. Zhang, J. Jin, L. Yang, and N. Jing, "Compact wideband SIW horn antenna fed by elevated-CPW structure," *IEEE Trans. Antennas Propag.*, vol. 63, no. 10, pp. 4551–4557, Jul. 2015.

[28] A. R. Mallahzadeh and S. Esfandiarpour, "Wideband H-plane horn antenna based on ridge substrate integrated waveguide (RSIW)," *IEEE Antennas Wirel. Propag. Lett.*, vol. 11, pp. 85–88, Jan. 2012.

[29] L. Wang, M. Garcia-Vigueras, M. Alvarez-Folgueiras, and J. R. Mosig, "Wideband H-plane dielectric horn antenna," *IET Microw. Antennas Propag.*, vol. 11, no. 12, pp. 1695–1701, Apr. 2017.

[30] Y. Cao, Y. Cai, C. Jin, Z. Qian, L. Zhu, and W. Zhang, "Broadband SIW horn antenna loaded with offset double-sided parallel-strip lines," *IEEE Antennas Wirel. Propag. Lett.*, vol. 17, no. 9, pp. 1740–1744, Aug. 2018.

[31] Y. Cai, Y. Zhang, L. Yang, Y. Cao, and Z. Qian, "Design of low-profile metamaterial-loaded substrate integrated waveguide horn antenna and its array applications," *IEEE Trans. Antennas Propag.*, vol. 65, no. 7, pp. 3732–3737, May 2017.

[32] C. Segura-Gómez, Palomares-Caballero, A. Alex-Amor, J. Valenzuela-Valdés, and P. Padilla, "Modular design for a stacked siw antenna array at ka-band," *IEEE Access*, vol. 8, pp. 158 568–158 578, Aug. 2020.

[33] L. Liu, T. Bai, J. Deng, D. Sun, Y. Zhang, T. Yong, S. Zhou, and L. Guo, "Substrate integrated waveguide filtering horn antenna facilitated by embedded via-hole arrays," *IEEE Antennas and Wireless Propagation Letters*, vol. 19, no. 7, pp. 1187–1191, May 2020.

[34] L. Wang, M. Esquius-Morote, H. Qi, X. Yin, and J. R. Mosig, "Phase corrected h-plane horn antenna in gap siw technology," *IEEE Transactions on Antennas and Propagation*, vol. 65, no. 1, pp. 347–353, Nov. 2017.

[35] H. Li, Y. Li, L. Chang, W. Sun, X. Qin, and H. Wang, "Wideband dual-polarized endfire antenna array with overlapped apertures and small clearance for 5g millimeter wave applications," *IEEE Transactions on Antennas and Propagation*, pp. 1–1, Aug. 2020.

[36] J. Zhang, K. Zhao, L. Wang, S. Zhang, and G. F. Pedersen, "Dual-polarized phased array with end-fire radiation for 5G handset applications," *IEEE Trans. Antennas Propag.*, vol. 68, no. 4, pp. 3277–3282, Sep. 2020.

[37] M. Esquius-Morote, B. Fuchs, J. Zürcher, and J. R. Mosig, "A printed transition for matching improvement of SIW horn antennas," *IEEE Trans. Antennas Propag.*, vol. 61, no. 4, pp. 1923–1930, Dec. 2013.

[38] "User Equipment (UE) Radio Transmission and Reception; Part 2: Range 2 Standalone (Release 16), document TS38.101-2 v16.3.1," Tech. Rep., Apr. 2020.